THE JOURNAL OF PHYSICAL CHEMISTRY LETTERS
A JOURNAL OF THE AMERICAN CHEMICAL SOCIETY

pubs.acs.org/JPCL Letter

Electrochemical Nitrate Reduction to Ammonia Driven by Catalytic Monovacancies in Single-Walled Carbon Nanotubes

Jana Jelušić,[§] Nia J. Harmon,[§] Jan Paul Menzel, Shize Yang, Quentin C. Bertrand, Hailiang Wang, Gary W. Brudvig, and Victor S. Batista*

Cite This: https://doi.org/10.1021/acs.jpclett.6c00219 Read Online

ACCESS | Metrics & More | Article Recommendations | Supporting Information

ABSTRACT: Developing alternative routes for ammonia (NH_3) synthesis from nitrogen-containing species under mild conditions is a central challenge in sustainable catalysis. Single-walled carbon nanotubes (SWCNTs) containing intrinsic monovacancy defects provide a distinct class of active sites for electrochemical ammonia (NH_3) production. Here, we investigate the reactivity of SWCNT monovacancies in the electrochemical reduction of nitrate (NO_3^-), nitrite (NO_2^-), and hydroxylamine (NH_2OH) to NH_3. We find that NO_3^- and NO_2^- reduction proceeds through a single proton-coupled electron transfer (PCET) pathway that requires regeneration of the vacancy site. In contrast, NH_2OH reduction can occur through both vacancy-dependent and vacancy-independent mechanisms. At more negative potentials, NH_2OH reacts at the regenerated vacancy to form either a ketone and NH_3 or an oxime intermediate, which subsequently yields NH_3 through additional PCET steps. These results establish SWCNT monovacancies as well-defined model systems for probing reaction mechanisms and guiding the design of efficient electrocatalysts for nitrate-to-ammonia conversion.

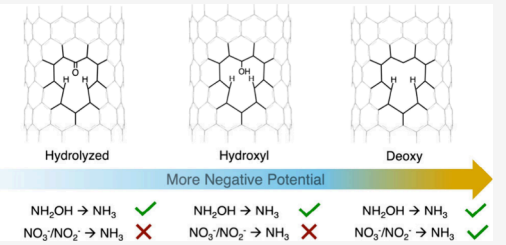

Ammonia (NH_3) is an attractive renewable fuel due to its ability to be stored and transported as a liquid, and its high energy density of 391 kJ/mol.[1] This energy density enables efficient energy release through thermal decomposition or electrochemical conversion to nitrogen gas (N_2). For most of Earth's history, NH_3 production was governed by biological nitrogen fixation.[2] Over the past century, industrial nitrogen fixation has become the dominant source, driven primarily by the demand for nitrogen-based fertilizers.[3] As both an essential fertilizer and a potential carbon-free energy carrier, ammonia plays a central role in advancing sustainable energy and food production.

However, extensive fertilizer use has resulted in significant accumulation of nitrogen-containing compounds and ammonia in the environment. Ammonia is processed by soil microorganisms through nitrification and denitrification into nitrate (NO_3^-),[4] which readily leaches into groundwater and surface water. Elevated nitrate concentrations pose serious human health risks, including blood disorders and increased cancer incidence,[5] and promote eutrophication by stimulating algal blooms, leading to widespread ecological damage.[6]

Conventional strategies for nitrate remediation—such as ion exchange, biological denitrification, and reverse osmosis—are effective but often energy-intensive and generate secondary waste streams.[7] In contrast, electrochemical nitrate reduction powered by renewable electricity offers a sustainable pathway to recycle nitrate into value-added products, including ammonia, hydroxylamine (NH_2OH), or dinitrogen.

Most efficient electrocatalysts for nitrate reduction rely on precious metals, motivating the search for metal-free alternatives. Carbon-based electrocatalysts are appealing due to their chemical stability and resistance to metal leaching. Carbon nanotubes (CNTs), in particular, exhibit exceptional thermal and hydrothermal stability, low porosity, and high surface area.[8] Recent work by Wang and co-workers[9] demonstrated that pristine CNTs can catalyze the electrochemical NO_3^- reduction reaction (NO_3RR) directly on native carbon surfaces. This finding challenges the widely held assumption that heteroatom doping is necessary to activate carbon-based catalysts.[10−12] Notably, oxygen- and nitrogen-containing functional groups were shown to suppress NO_3RR activity, suggesting that a distinct catalytic mechanism operates on pristine carbon. Despite these advances, the elementary reaction pathways responsible for nitrate reduction on carbon surfaces remain poorly defined. Recent studies further emphasize the importance of well-defined active-site architectures and structure−reactivity relationships in nitrogen-cycle electrosynthesis, including defect-engineered and tandem catalytic systems.[13,14]

To address this knowledge gap, we combine electrochemical measurements with density functional theory (DFT) calculations to elucidate the role of single-atom vacancies in single-

Received: January 22, 2026
Revised: February 24, 2026
Accepted: February 26, 2026

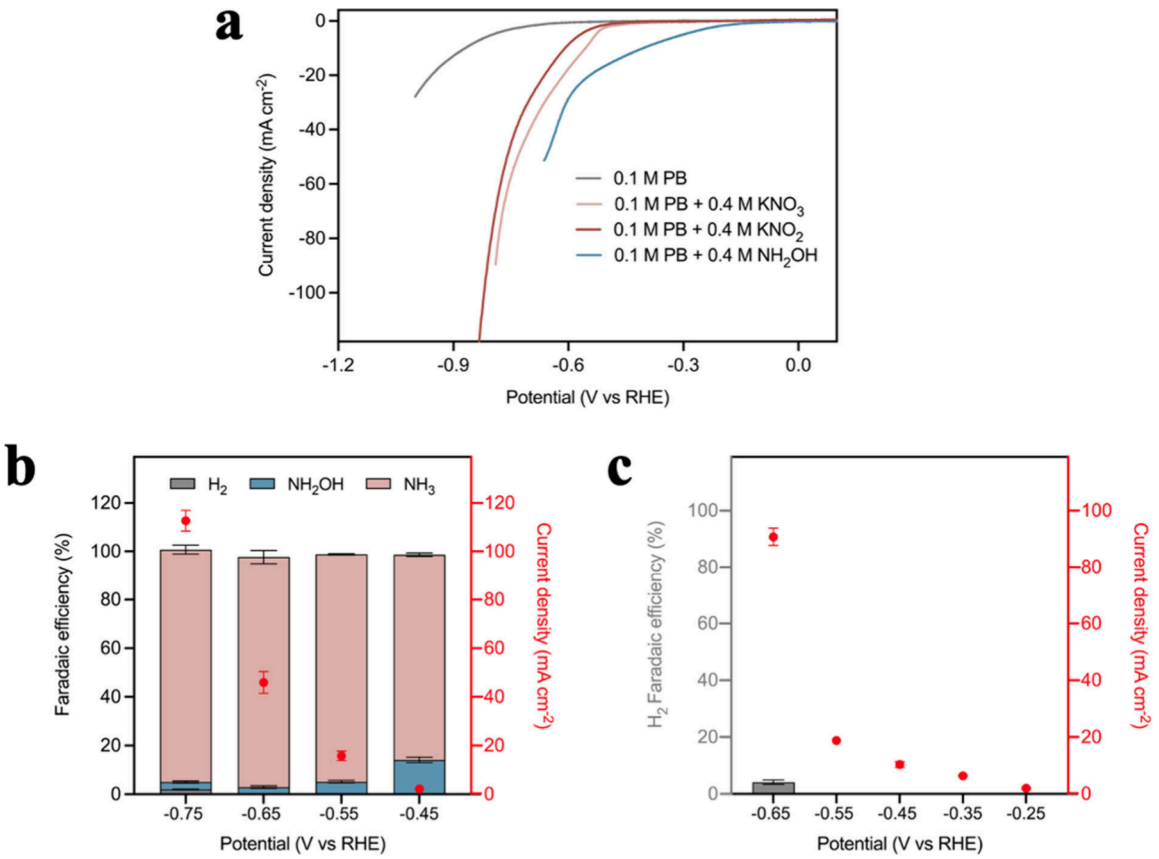

Figure 1. Electrocatalytic performance of SWCNTs. (a) LSV diagrams of SWCNTs recorded at a scan rate of 5 mV s^{-1} in an Ar-saturated electrolyte (pH 7.2). (b) Potential-dependent NO_2RR performance of SWCNTs in Ar-saturated 0.1 M PB containing 0.4 M KNO_2 (pH 7.2). (c) Potential-dependent NH_2OHRR performance of SWCNTs in Ar-saturated 0.1 M PB containing 0.4 M NH_2OH (pH 7.2). Error bars denote standard deviations from at least three independent measurements; some error bars do not appear because they are smaller than the size of the symbol.

walled carbon nanotubes (SWCNTs) during the electrochemical reduction of nitrate, nitrite, and hydroxylamine. Building on our previous work,[15] which demonstrated that single-atom vacancies in SWCNTs behave as carbene-like reactive centers capable of electrochemical regeneration, we now show that these monovacancies can catalyze the electrochemical reduction of NO_3^-, NO_2^-, and NH_2OH to NH_3.

The SWCNT catalyst material was prepared following prior work[9] and drop-cast onto carbon fiber paper (CFP) to produce cathodes (Figure S1). High-resolution transmission electron microscopy (TEM) was used to characterize the nanotube samples (Figure S2). The images reveal bundled SWCNTs, with individual tubes clearly resolved and exhibiting diameters of approximately 1 nm. Consistent with previous reports, residual Fe species remain even after purification and are visible in TEM images. Although residual Fe is visible in TEM, prior work using the same SWCNT material and purification protocol showed no detectable surface Fe by Fe 2p XPS and concluded that remaining Fe is encapsulated rather than exposed. In that work, control experiments further showed that Fe deposited on CFP loses most nitrate reduction activity after the same HCl and H_2O_2 treatment, and postelectrolysis XPS confirmed that Fe does not migrate to the SWCNT surface under operating conditions.[9]

We first compared the catalytic performance of SWCNTs toward the electrochemical reduction of NO_3^-, NO_2^- (NO_2RR), and NH_2OH (NH_2OHRR). Electrochemical measurements were conducted in a two-compartment H-cell using Ar-saturated 0.1 M phosphate buffer (PB), with or without KNO_3, KNO_2, or NH_2OH. Nitrite and hydroxylamine were selected because they are proposed intermediates in the reaction pathway from nitrate to ammonia.

To determine the onset potential for each reaction, we recorded linear sweep voltammograms (LSVs) (Figure 1a), and the extracted values are summarized in Table S1. Among the three nitrogen species, SWCNTs were most active for NH_2OHRR, which exhibited an onset potential of −0.15 V versus the reversible hydrogen electrode (RHE). Unless otherwise noted, all potentials reported herein are referenced to the RHE scale. In contrast, the onset potentials for NO_3RR and NO_2RR were substantially more negative (−0.44 V and −0.49 V, respectively), indicating higher energy barriers for these reactions on the SWCNT surface. LSVs for each nitrogen-containing electrolyte and the corresponding phosphate-buffer controls are provided in Figures S3−S5.

We then performed 1-h controlled potential electrolysis (CPE) in PB electrolyte containing either NO_2^- (Figure 1b) or NH_2OH (Figure 1c). Gas chromatography detected hydrogen (H_2), as the only gaseous product; nitric oxide (NO), nitrous oxide (N_2O), and N_2 were not observed under any tested conditions. Liquid-phase products (NH_2OH and NH_3) were quantified after electrolysis by colorimetric assays (Figure S6). In 0.1 M PB + 0.4 M NH_2OH, however, NH_3 could not be

https://doi.org/10.1021/acs.jpclett.6c00219
J. Phys. Chem. Lett. XXXX, XXX, XXX−XXX

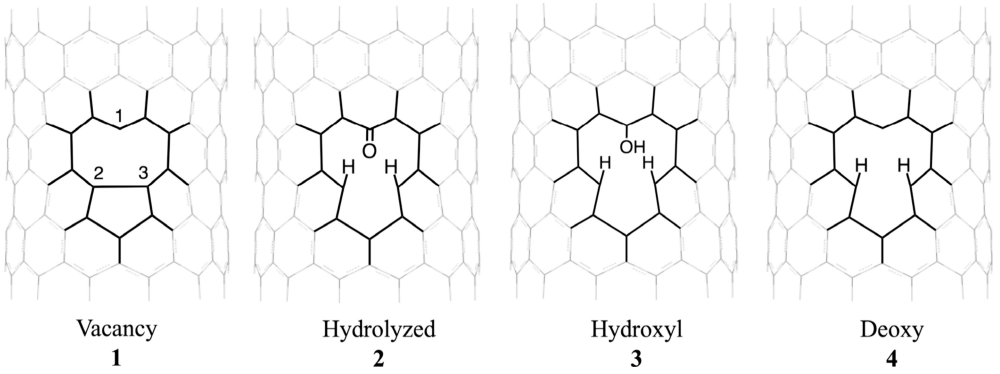

Figure 2. Key SWCNT vacancy structures involved in the catalytic cycle. Schematic representation of the evolution of a SWCNT monovacancy from hydrolyzed to deoxygenated forms. Structure **1** denotes the pristine monovacancy and defines the carbon atom numbering scheme. Structure **2** corresponds to the hydrolyzed vacancy, featuring a keto group at C-1 and C−H bonds at C-2 and C-3. Structure **3** is the one-electron/one-proton reduced hydroxylated vacancy. Structure **4** is the fully deoxygenated vacancy, with C−H bonds at C-2 and C-3.

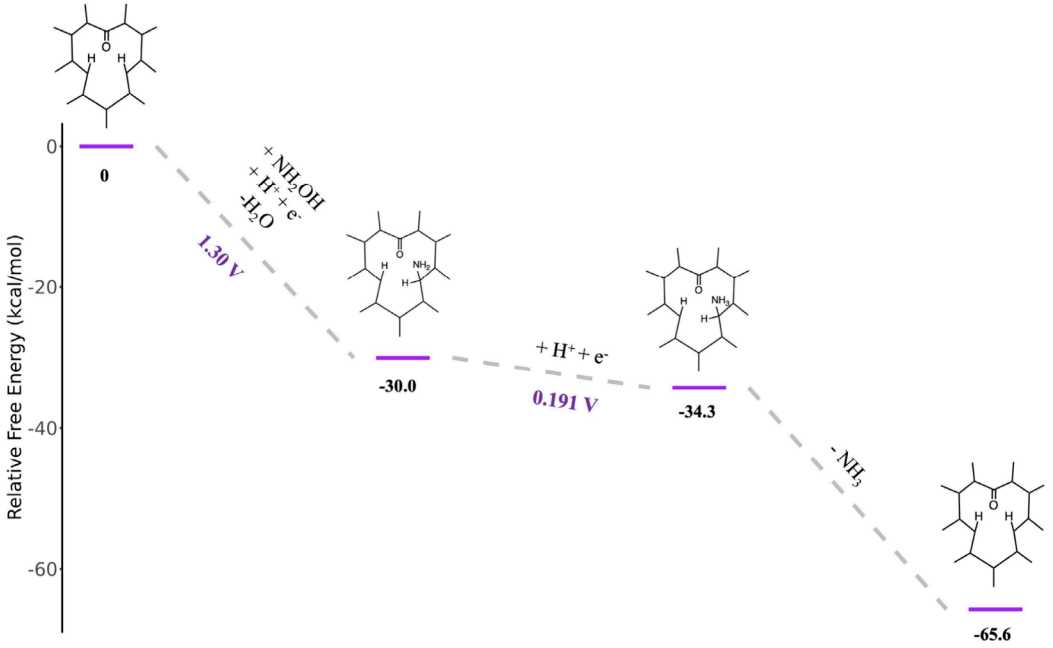

Figure 3. NH_2OH reduction pathway under mild potentials. Schematic illustration of the NH_2OH reduction mechanism operative at low overpotentials, in which the SWCNT vacancy remains hydrolyzed and facilitates stepwise PCET-driven conversion to NH_3. Energy diagram created with EveRplot.[18]

quantified reliably by the indophenol blue method. We, therefore, quantified H_2 by gas chromatography, which remains sensitive at low current densities (Figure S7) and assigned the faradaic efficiency (FE) to NH_3, given that H_2 and NH_3 are the only expected products.

As a benchmark, the original NO_3RR study in 0.1 M PB + 0.4 M KNO_3 (pH 7.2) reported high NH_3 selectivity from −0.55 V to −0.85 V, with <10% FE attributed to NO_2^- and H_2. At −0.85 V, the maximum NH_3 FE reached ∼90% with a total current density of 63 mA cm^{-2}. Under the present conditions (0.1 M PB + 0.4 M KNO_2, pH 7.2), we observed a similar selectivity window: SWCNTs favored NH_3 from −0.45 V to −0.75 V, achieving a maximum NH_3 FE of ∼96% and a total current density of 113 mA cm^{-2} at −0.75 V. Notably, NH_2OH was detected during NO_2^- electroreduction, providing experimental support for NH_2OH as an intermediate in route to NH_3. Although NH_2OH was not observed in the prior NO_3RR study,[9] we hypothesize that it was formed on the SWCNT surface but rapidly reduced to NH_3, making the detection difficult.

We then examined NH_2OH electroreduction in 0.1 M PB + 0.4 M NH_2OH (pH 7.2). Across −0.25 V to −0.55 V, no H_2 was detected, indicating ∼100% FE toward NH_3 over this range, consistent with prior observations.[9] Competition from the hydrogen evolution reaction (HER) emerged only at the most negative potential tested (−0.65 V), where H_2 accounted for ∼4% FE.

Consistent with these results, the LSVs (Figure 1a) show enhanced cathodic currents upon addition of each nitrogen species relative to the background electrolyte, confirming electrochemical reduction. The similar onset potentials for NO_3RR (−0.44 V) and NO_2RR (−0.49 V) suggest that both processes share a potential-dependent activation threshold, whereas NH_2OHRR initiates at a much milder bias (≈ −0.15 V).

To rationalize these experimental observations and uncover the structural and electronic factors underlying the observed

https://doi.org/10.1021/acs.jpclett.6c00219
J. Phys. Chem. Lett. XXXX, XXX, XXX−XXX

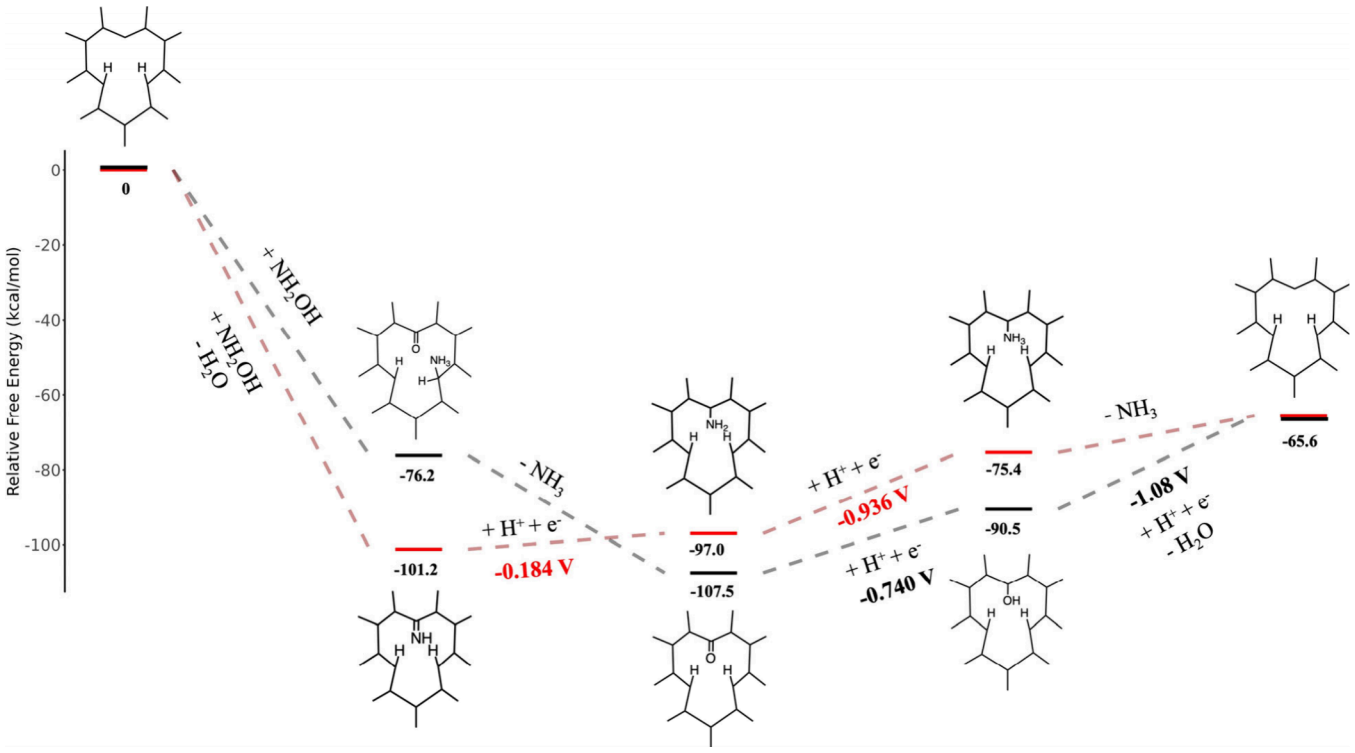

Figure 4. Alternative NH_2OH reduction pathways at regenerated vacancies. Comparison of NH_2OH reduction pathways that become accessible once the SWCNT vacancy is regenerated under more negative potentials. In the first pathway (black), NH_2OH forms a keto group at C-1 and forms an NH_3-bound intermediate at C-3. In the second pathway (red), NH_2OH reacts at C-1 to form an oxime intermediate. Energy diagram created with EveRplot.[18]

onset potentials, we next performed DFT calculations on representative SWCNT vacancy structures (Figure 2). We mapped potential-dependent transformations of hydrolyzed, hydroxylated, and deoxygenated vacancies and evaluated how these sites mediate reductions of NO_3^-, NO_2^-, and NH_2OH to NH_3. The calculations indicate that SWCNT vacancies are the key active sites for nitrate-to-ammonia conversion, with NO_3^-/NO_2^- reduction proceeding through a unified pathway involving vacancy regeneration. For NH_2OH reduction, the DFT modeling reveals two potential-dependent routes leading to the formation of NH_3. While the precise microscopic mechanism cannot yet be assigned, this interpretation provides a consistent framework that links the onset ordering with the computed redox energetics of the vacancy ladder. Electrochemical free energies were evaluated within a continuum solvation framework (polarizable continuum model, PCM).[16,17] Explicit solvent structure and interfacial double-layer electric field effects were not modeled; accordingly, the reported potentials correspond to thermodynamic equilibrium thresholds rather than field-dependent kinetic barriers. Additional computational details, including the electronic- and free-energy formalism used to compute redox potentials, are provided in the Supporting Information.

When the applied potential is insufficient to drive the two proton-coupled electron transfer (PCET) steps required to convert Structure **2** into the fully deoxygenated Structure **4** (Figure 2), complete vacancy deoxygenation is suppressed. Under these conditions, NH_2OH can nevertheless be reduced to NH_3 via an alternative pathway (Figure 3). In this mechanism, the monovacancy first undergoes hydrolysis to form a ketone at C-1 with C−H bonds at C-2 and C-3 (Structure **2**, Figure 2). NH_2OH then participates in a PCET step, during which an NH_2 group binds at C-3 with concomitant water release. From either the hydrolyzed (Structure **2**) or hydroxylated (Structure **3**) vacancy, the adsorbed NH_2 species undergoes a final PCET-driven hydrogenation to release NH_3, consistent with the step occurring at $E_{RHE} \approx 0.19$ V (eq 1 and Figure 3).

The pathway proceeding via the hydroxyl intermediate (Structure **3**) yields the overall stoichiometry summarized in eq 1:

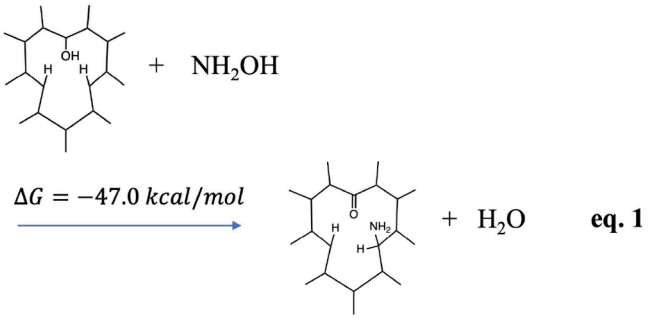

eq. 1

At higher overpotentials, once the deoxygenated vacancy (Structure **4**) begins to form, NH_2OH can engage in two competing pathways: one leading to formation of a ketone intermediate and NH_3, and another proceeding through an oxime species (Figure 4). The need to generate the deoxygenated vacancy is consistent with the more negative onset potentials observed for NO_3RR and NO_2RR relative to NH_2OHRR, even though these reactions likely initiate while the surface is still largely oxygenated.

In the oxime pathway, NH_2OH attacks the vacancy at C-1, forming an oxime intermediate with consequent water release.

https://doi.org/10.1021/acs.jpclett.6c00219
J. Phys. Chem. Lett. XXXX, XXX, XXX−XXX

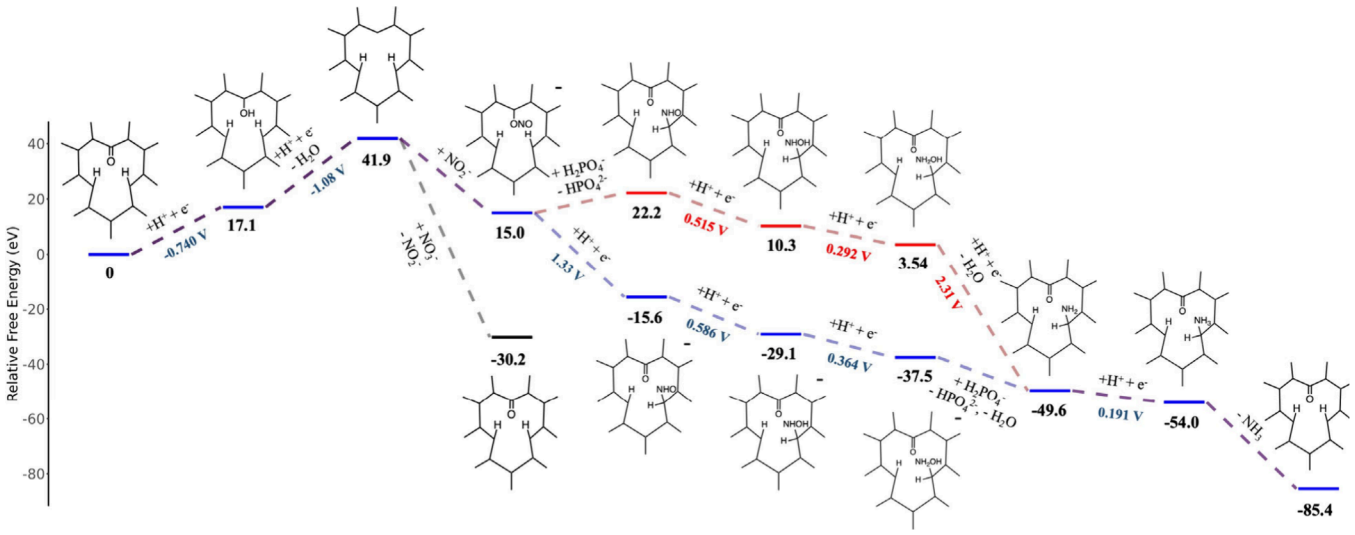

Figure 5. Analogous NO_3^- and NO_2^- reduction pathways at regenerated vacancies. Schematic representation of NO_3^- and NO_2^- reduction mechanisms that require formation of the regenerated (deoxygenated) vacancy. In the red pathway, NO_3^- binds at C-1 to form a ketone, releasing NO_2^-, which is subsequently reduced through sequential steps to NH_3. In the blue pathway, successive PCET steps generate a ketone at C-1 and an NH_2OH intermediate at C-3, which is further hydrogenated to yield NH_3. Energy diagram created with EveRplot.[18]

The first PCET step, corresponding to initial N−H hydrogenation, occurs at a relatively mild potential (E_{RHE} = −0.18 V), whereas the subsequent PCET step requires a more negative potential (E_{RHE} = −0.94 V). Release of NH_3 from the oxime-derived intermediate is energetically uphill by 9.8 kcal/mol. However, NH_3 can be displaced by an incoming hydroxylamine molecule, thereby completing the catalytic cycle.

As shown in Figure 4, the DFT-computed PCET landscape for hydroxylamine reduction spans −0.18 to −0.94 V vs RHE, covering oxime hydrogenation and NH_2 formation on the deoxygenated vacancy. This range defines the thermodynamic window in which NH_2OH-derived intermediates become catalytically accessible and partially overlaps with the potentials where NO_3^- and NO_2^- reduction currents appear experimentally. The overlap indicates that catalytic turnover can begin once a fraction of vacancies undergoes partial reduction, even though full deoxygenation (Structure **4**) is thermodynamically favored only at substantially higher bias, consistent with the calculated −1.08 V threshold.

In the absence of NH_2OH, reduction of NO_2^- and NO_3^- requires prior formation of the deoxygenated vacancy (Structure **4**). NO_3^- initially binds at the C-1 site of Structure **4**, yielding Structure **2** along with NO_2^- release; NO_2^- can then adsorb analogously on Structure **4** (Figure 5). The pathway shown in red corresponds to the energetically accessible sequence in which nitrogen is protonated first, leading to ketone formation at C-1 and migration of the NHO group to C-3. Subsequent PCET steps are exothermic, producing NH_3 at C-3 and regenerating Structure **2**. In contrast, the mechanism shown in blue represents a series of PCET steps prior to NH_2OH protonation, ultimately forming the same intermediate, an NH_2 group bound at C-3, along with water.

The observation that NO_3^- and NO_2^- reduction onsets occur at potentials substantially more positive than that required for full vacancy deoxygenation (≈ −1.08 V; Structure **4**), as well as more positive than the −0.740 V threshold associated with conversion of the oxygenated vacancy to the hydrolyzed intermediate, indicates that the early currents are unlikely to originate from catalysis at pre-existing deoxygenated vacancies. Instead, they likely arise from outer-sphere or partially coupled electron-transfer processes involving NO_3^-/NO_2^- in the interfacial region adjacent to the oxygenated SWCNT surface.[19,20] In an outer-sphere process, the reactant does not form a direct chemical bond with the electrode; rather, the electron tunnels across the solvent-electrode interface to a species that remains solvated and weakly coupled to the surface.[19−21] Such reactions are typically electron-transfer-limited, meaning that the rate is governed by the speed of charge tunneling rather than by adsorption or mass transport.[19,20] Consequently, the observed onset potential primarily reflects the intrinsic electronic coupling between the SWCNT surface and the solution-phase reactant as well as the applied overpotential required to achieve a measurable current density (1 mA cm^{-2}, Table S1).

Importantly, the potentials later derived from DFT represent equilibrium thermodynamic thresholds for sequential PCET-driven vacancy reduction, whereas the experimental onsets correspond to the kinetic bias at which measurable current first appears. The several hundred millivolt difference between the calculated deoxygenation potential and the experimental onsets does not indicate a discrepancy; rather, it suggests that charge transfer can occur before full thermodynamic vacancy reduction is achieved. Although detailed kinetic parameters are not yet available, this interpretation is consistent with well-established outer-sphere electron-transfer behavior on carbon electrodes, where tunneling through the interfacial electric field controls the reaction rate.[19−22] As the applied potential becomes more negative and approaches the −0.740 V threshold, progressive surface reduction increases the population of partially reduced vacancy states, and at still higher bias (≈ −1.08 V), adsorption-mediated pathways involving the fully deoxygenated vacancy become dominant. Such kinetic-thermodynamic offsets are common in proton-coupled electrocatalytic systems and naturally explain why measurable currents emerge at milder potentials than those predicted by equilibrium thermodynamic potentials.

https://doi.org/10.1021/acs.jpclett.6c00219
J. Phys. Chem. Lett. XXXX, XXX, XXX−XXX

This quantitative correspondence between experiment and theory strengthens the proposed mechanistic interpretation. In particular, the experimentally observed, nearly identical onset potentials for NO_3RR and NO_2RR (Table S1) support a common underlying process. Both reactions proceed most efficiently once vacancy regeneration becomes thermodynamically accessible; however, partial reduction of the surface likely enables an initial current at milder potentials, where transiently reduced oxygenated vacancies remain catalytically competent. This framework reconciles the apparent potential mismatch between experiment and computation without invoking a distinct low-energy active site and reinforces vacancy regeneration as the potential-limiting step in the overall nitrate-to-ammonia reduction pathway.

While the DFT analysis identifies the fully deoxygenated vacancy (Structure **4**) as the thermodynamically favored active state at sufficiently negative bias, direct spectroscopic confirmation of vacancy deoxygenation under operating electrochemical conditions has not yet been obtained. The present mechanistic interpretation is therefore based on the consistency between computed regeneration thresholds, experimentally observed onset ordering, and product selectivity trends. Operando spectroscopic characterization of vacancy states during electrolysis would provide valuable future validation of the proposed mechanism.

In this study, we demonstrated that monovacancy defects in SWCNTs mediate the electrochemical reduction of NO_3^-, NO_2^-, and NH_2OH to NH_3 through distinct yet interconnected reaction pathways. Reduction of NO_3^- and NO_2^- requires vacancy regeneration, whereas NH_2OH reduction can proceed through either vacancy-dependent or vacancy-independent routes, depending on the applied potential. The nearly identical onset potentials observed for NO_3RR and NO_2RR, together with the computed energetics of vacancy-regeneration, indicate that both reactions are governed by a common potential-dependent activation framework. In this picture, initial activity arises from partially reduced, oxygenated vacancies, while sustained turnover at higher overpotentials is enabled by fully regenerated deoxygenated sites. In contrast, NH_2OHRR proceeds via a vacancy-independent mechanism at significantly milder potentials.

Together, these findings establish SWCNT vacancies as the key active sites governing activity and selectivity in nitrogen-species electroreduction and provide a unified mechanistic framework for understanding nitrate-to-ammonia conversion on defect-engineered carbon materials. By directly linking catalytic performance to the thermodynamics of vacancy regeneration, this framework offers general principles for tuning defect density and redox accessibility in carbon nanomaterials and can be extended to other carbon-based or hybrid metal−carbon architectures to guide the development of selective, energy-efficient, and sustainable nitrogen-conversion catalysts.

■ ASSOCIATED CONTENT

Supporting Information

The Supporting Information is available free of charge at https://pubs.acs.org/doi/10.1021/acs.jpclett.6c00219.

Details of the theoretical calculations are also included, covering interactions with pristine and hydroxylated nanotube structures, along with the DFT-optimized coordinates for all reported nanotube models; the optimized structures are provided as a compressed archive (ZIP)

Detailed descriptions of the experimental procedures, including catalyst synthesis, materials characterization, electrode fabrication, electrolyte preparation, electrochemical measurements, and product quantification; additional data include SEM and TEM images, LSV curves, UV−vis spectra, calibration plots, and tabulated onset potentials (PDF)

■ AUTHOR INFORMATION

Corresponding Author

Victor S. Batista − *Department of Chemistry, Yale University, New Haven, Connecticut 06520, United States; Yale Energy Sciences Institute, Yale University, West Haven, Connecticut 06516, United States;* orcid.org/0000-0002-3262-1237; Email: victor.batista@yale.edu

Authors

Jana Jelušić − *Department of Chemistry, Yale University, New Haven, Connecticut 06520, United States; Yale Energy Sciences Institute, Yale University, West Haven, Connecticut 06516, United States;* orcid.org/0000-0003-1183-5954

Nia J. Harmon − *Department of Chemistry, Yale University, New Haven, Connecticut 06520, United States; Yale Energy Sciences Institute, Yale University, West Haven, Connecticut 06516, United States;* orcid.org/0000-0002-4117-4088

Jan Paul Menzel − *Department of Chemistry, Yale University, New Haven, Connecticut 06520, United States; Yale Energy Sciences Institute, Yale University, West Haven, Connecticut 06516, United States;* orcid.org/0000-0002-1312-5000

Shize Yang − *Yale Energy Sciences Institute, Yale University, West Haven, Connecticut 06516, United States;* orcid.org/0000-0002-0421-006X

Quentin C. Bertrand − *Department of Chemistry, Yale University, New Haven, Connecticut 06520, United States*

Hailiang Wang − *Department of Chemistry, Yale University, New Haven, Connecticut 06520, United States; Yale Energy Sciences Institute, Yale University, West Haven, Connecticut 06516, United States;* orcid.org/0000-0003-4409-2034

Gary W. Brudvig − *Department of Chemistry, Yale University, New Haven, Connecticut 06520, United States; Yale Energy Sciences Institute, Yale University, West Haven, Connecticut 06516, United States;* orcid.org/0000-0002-7040-1892

Complete contact information is available at: https://pubs.acs.org/10.1021/acs.jpclett.6c00219

Author Contributions

[§]J.J., N.J.H.: These authors contributed equally to this work.

Notes

The authors declare no competing financial interest.

■ ACKNOWLEDGMENTS

The authors acknowledge support by the US Department of Energy, Chemical Sciences, Geosciences, and Biosciences Division, 766 Office of Basic Energy Sciences, Office of Science (Grant DE767 FG02-07ER15909). N.J.H. acknowledges the National Science Foundation Graduate Research Fellowship.

REFERENCES

(1) Liu, H.-Y.; Lant, H. M. C.; Cody, C. C.; Jelušić, J.; Crabtree, R. H.; Brudvig, G. W. Electrochemical Ammonia Oxidation with Molecular Catalysts. *ACS Catal.* **2023**, *13* (7), 4675−4682.

(2) Li, W.; Zhang, S.; Ding, J.; Liu, J.; Wang, Z.; Zhang, H.; Ding, J.; Chen, L.; Liang, C. Sustainable Nitrogen Fixation to Produce Ammonia by Electroreduction of Plasma-Generated Nitrite. *ACS Sustain. Chem. Eng.* **2023**, *11* (3), 1168−1177.

(3) Vitousek, P. M.; Menge, D. N. L.; Reed, S. C.; Cleveland, C. C. Biological Nitrogen Fixation: Rates, Patterns and Ecological Controls in Terrestrial Ecosystems. *Philos. Trans. R. Soc. B* **2013**, *368* (1621), 20130119.

(4) Wang, X.; Bai, J.; Xie, T.; Wang, W.; Zhang, G.; Yin, S.; Wang, D. Effects of Biological Nitrification Inhibitors on Nitrogen Use Efficiency and Greenhouse Gas Emissions in Agricultural Soils: A Review. *Ecotoxicol. Environ. Saf.* **2021**, *220*, 112338.

(5) Ward, M. H.; Jones, R. R.; Brender, J. D.; de Kok, T. M.; Weyer, P. J.; Nolan, B. T.; Villanueva, C. M.; van Breda, S. G. Drinking Water Nitrate and Human Health: An Updated Review. *Int. J. Environ. Res. Public Health.* **2018**, *15* (7), 1557.

(6) Akinnawo, S. O. Eutrophication: Causes, Consequences, Physical, Chemical and Biological Techniques for Mitigation Strategies. *Environ. Chall.* **2023**, *12*, 100733.

(7) Shrimali, M.; Singh, K. P. New Methods of Nitrate Removal From Water. *Environ. Pollut.* **2001**, *112* (3), 351−359.

(8) Li, Y.; Maruyama, S. *Single-Walled Carbon Nanotubes: Preparation, Properties and Applications*; Springer International Publishing: 2019.

(9) Harmon, N. J.; Rooney, C. L.; Tao, Z.; Shang, B.; Raychaudhuri, N.; Choi, C.; Li, H.; Wang, H. Intrinsic Catalytic Activity of Carbon Nanotubes for Electrochemical Nitrate Reduction. *ACS Catal.* **2022**, *12* (15), 9135−9142.

(10) Xu, X.; Jiang, S.; Hu, Z.; Liu, S. Nitrogen-Doped Carbon Nanotubes: High Electrocatalytic Activity toward the Oxidation of Hydrogen Peroxide and Its Application for Biosensing. *ACS Nano* **2010**, *4* (7), 4292−4298.

(11) Gong, K.; Du, F.; Xia, Z.; Durstock, M.; Dai, L. Nitrogen-Doped Carbon Nanotube Arrays with High Electrocatalytic Activity for Oxygen Reduction. *Science* **2009**, *323* (5915), 760−764.

(12) Zhao, Y.; Nakamura, R.; Kamiya, K.; Nakanishi, S.; Hashimoto, K. Nitrogen-Doped Carbon Nanomaterials as Non-Metal Electrocatalysts for Water Oxidation. *Nat. Commun.* **2013**, *4* (1), 2390.

(13) Sun, Z.; Niu, R.; Shang, S.; Guo, Y.; Zhang, H.; Liu, X.; Feng, L.; Chu, K. Plasma-Electrocatalytic Synthesis of Urea From Air and CO_2. *Nat. Commun.* **2025**, *16* (1), 8837.

(14) Chen, K.; Ma, D.; Zhang, Y.; Wang, F.; Yang, X.; Wang, X.; Zhang, H.; Liu, X.; Bao, R.; Chu, K. Urea Electrosynthesis from Nitrate and CO_2 on Diatomic Alloys. *Adv. Mater.* **2024**, *36* (30), 2402160.

(15) Jelušić, J.; Menzel, J. P.; Bertrand, Q. C.; Crabtree, R. H.; Wang, H.; Brudvig, G. W.; Batista, V. S. Modeling Electrochemical Vacancy Regeneration in Single-Walled Carbon Nanotubes. *J. Phys. Chem. Lett.* **2024**, *15* (30), 7788−7792.

(16) Improta, R.; Barone, V.; Scalmani, G.; Frisch, M. J. A State-Specific Polarizable Continuum Model Time Dependent Density Functional Theory Method for Excited State Calculations in Solution. *J. Chem. Phys.* **2006**, *125* (5), 054103.

(17) Improta, R.; Scalmani, G.; Frisch, M. J.; Barone, V. Toward Effective and Reliable Fluorescence Energies in Solution by a New State Specific Polarizable Continuum Model Time Dependent Density Functional Theory Approach. *J. Chem. Phys.* **2007**, *127* (7), 074504.

(18) Bogdos, M. K.; Morandi, B. EveRplot: A Web-Based Shiny Application for Creating Energy vs Reaction Coordinate Diagrams. *J. Chem. Educ.* **2023**, *100* (9), 3641−3644.

(19) McCreery, R. L. Advanced Carbon Electrode Materials for Molecular Electrochemistry. *Chem. Rev.* **2008**, *108* (7), 2646−2687.

(20) Unwin, P. R.; Güell, A. G.; Zhang, G. Nanoscale Electrochemistry of sp2 Carbon Materials: From Graphite and Graphene to Carbon Nanotubes. *Acc. Chem. Res.* **2016**, *49* (9), 2041−2048.

(21) Güell, A. G.; Cuharuc, A. S.; Kim, Y.-R.; Zhang, G.; Tan, S.-y.; Ebejer, N.; Unwin, P. R. Redox-Dependent Spatially Resolved Electrochemistry at Graphene and Graphite Step Edges. *ACS Nano* **2015**, *9* (4), 3558−3571.

(22) Cassidy, J. F.; de Carvalho, R. C.; Betts, A. J. Use of Inner/Outer Sphere Terminology in Electrochemistry—A Hexacyanoferrate II/III Case Study. *Electrochem* **2023**, *4* (3), 313−349.

https://doi.org/10.1021/acs.jpclett.6c00219
J. Phys. Chem. Lett. XXXX, XXX, XXX−XXX